



Relevance of transition turbulent model for hydrodynamic characteristics of low Reynolds number propeller

Suraj Pawar^{a,*}, Stefano Brizzolara^b

^a Department of Mechanical Engineering, Virginia Tech, Blacksburg, United States

^b Kevin T. Crofton Department of Aerospace and Ocean Engineering, Virginia Tech, Blacksburg, United States



ARTICLE INFO

Keywords:

Hydrodynamic analysis
Transition model
Open propeller
Ducted propeller

ABSTRACT

The propeller of an Autonomous Underwater Vehicle (AUV) operates at low Reynolds number in laminar to turbulent transition region. The performance of these propellers can be calculated accurately using RANSE solver with $\gamma - Re_\theta$ transition model. In this study, the global and local hydrodynamic characteristics of open and ducted propeller are investigated using the $\gamma - Re_\theta$ transition model. The capability of the $\gamma - Re_\theta$ transition model to capture laminar to turbulent transition on the surface of the open propeller is demonstrated by comparison with published experimental results. The application of transition model for the propeller $K_a=4.70$ inside the duct 19A shows that the centrifugal forces are dominant at low Reynolds number and the flow is mainly directed in the radial direction. The transition model is able to predict complex flow physics such as leading-edge separation, tip leakage vortex, and the separation bubble on outer surface of the duct. The accurate prediction of these flow phenomenon can lead to correct calculation of global hydrodynamic forces and moments acting on the propeller at low Reynolds number.

1. Introduction

The recent development in Autonomous Underwater Vehicles (AUV) for various missions such as seafloor mapping, detecting obstruction that can be a hazard to a commercial vessel and maritime security has lead to research on modeling flow around AUV and the propeller using CFD simulations [1]. Conventionally the flow analysis of the propeller is done using panel methods, especially at design advance coefficient. Higher order panel methods are needed for the calculation of the geometry of the wake sheet and accurate prediction of the tip vortex trajectory and pressure field [2]. This analysis is more challenging at off-design conditions because of the need for viscous corrections such as vortex wake alignment and strong coupling between boundary layer solvers to predict the separation [3]. At higher loading condition, the leading edge vortex passes over the propeller blade and significantly changes the load distribution and hence should be properly modeled [4]. The complexity increases when potential flow methods are used for modeling flow around ducted propellers. Baltazar et al. [5] showed that the hydrodynamic forces predicted using inviscid flow solver gets influenced by blade wake pitch, especially near the blade tip. RANSE solver on the other hand can predict unsteady pressure forces, cavitation, and flow transition correctly as demonstrated in several published literature. Hence, with an increase in computational

resources, RANSE solver is a valid approach for modeling flow around the propeller of an AUV.

Typically the Reynolds number of flow on the surface of the propeller of AUVs is in transitional flow regime $O(10^5)$, often lower than the minimum Reynolds number accepted by ITTC ($5 \cdot 10^5$). In this study, the flow around the model scale of the propeller is studied which also operates at the similar Reynolds number range using a transition model. Rhee and Joshi [6] validated the open water performance of a five-bladed highly skewed propeller P5168 using unstructured mesh-based Navier-Stokes solver with $k - \omega$ SST turbulent model and Reynolds Stress Transport turbulent model. Brizzolara et al. [7] systematically compared the global characteristics of a propeller, such as hydrodynamic coefficients as well as local characteristics such as pressure coefficient calculated using commercial RANSE solver CD-Adapco and in-house developed panel code for five standard test propeller. Hoekstra [8] developed a RANSE-based computational tool with the $k - \omega$ SST turbulent model for ducted propeller in which propeller was modeled as a virtual disk of finite thickness and the duct maintained its true shape. Bertetta et al. [9] predicted the open water performance, wake characteristics and cavitation of non-conventional CLT propeller using RANSE solver and compared the results with experimental data and results of panel method. Kinnas et al. [10] calculated the performance of ducted propeller subjected to uniform and inclined inflow using a

* Corresponding author.

E-mail address: surajp92@vt.edu (S. Pawar).

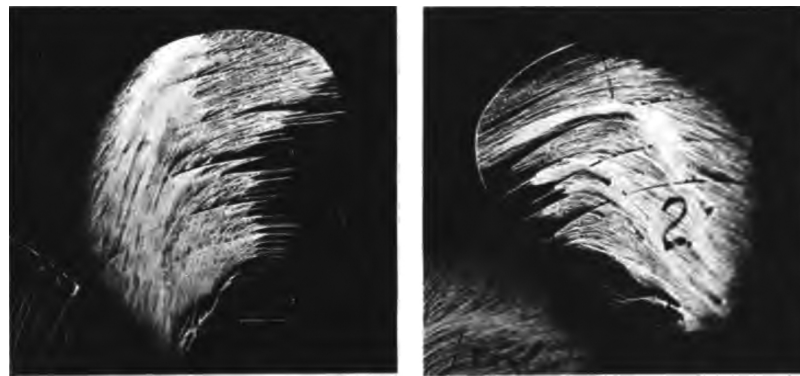


Fig. 1. Paint pattern on the surface of propeller. Left: suction; right: pressure [12].

hybrid method that couples potential flow solver with a viscous fluid solver. Majdfar et al. [11] studied the influence of duct angle and duct length on propeller's performance at different operating conditions using RANSE solver with fully turbulent model.

Generally, in many of the above numerical studies, the flow was modeled using turbulent model, which assumes that the flow is fully turbulent. Hence, these models cannot predict laminar to turbulent transition on the surface of a propeller that takes place at model scale. Kuiper [12] showed laminar to turbulent boundary layer transition taking place on the surface of propeller using paint test and UV-illumination images. Fig. 1 shows the typical paint patterns for the propeller at model scale. From paint test results, laminar to turbulent transition region can be detected by observing the direction of paint streak lines. In the laminar region, the paint streaks are directed radially outward due to dominant centrifugal force and in the turbulent region, paint streaks are directed in tangential direction due to dominant shear force. Hence the accuracy of hydrodynamic coefficients determined using RANSE solver decreases at high loading condition, i.e. lower advance ratio where the flow is in transition regime because of the assumption that flow is fully turbulent [6,13–15].

Even though the RANSE solver with fully turbulent model calculates hydrodynamic coefficients close to experimental results, there is still a room for improvement in prediction of thrust and torque coefficients of a propeller. Even though the flow on the surface of the model scale of the propeller is in the transition region, usually, this flow is modeled using fully turbulent models. The flow prediction around a propeller and hence hydrodynamic forces can be improved by using transition models. The $\gamma - Re_\theta$ transition model developed by Langtry et al. [16] is gaining popularity due to its ability to model transitional flow correctly. Malan et al. [17] successfully implemented $\gamma - Re_\theta$ transition model in commercial unstructured CFD code StarCCM+ [18] for several applications such as flow over the flat plate, airfoil and turbomachinery flows.

Müller et al. [15] calculated the thrust and torque coefficient of the skewed propeller at model scale using the combination of SST turbulence model and Local Correlation-based Transition Model. Bhattacharyya et al. [19] applied both $k - \omega$ SST turbulent model and $\gamma - Re_\theta$ transition model in commercial CFD code StarCCM+ to predict the flow around a propeller and found that the transition model is better in capturing laminar to turbulent transition region. Baltazar et al. [20] investigated propellers performance at model scale using both $k - \omega$ SST turbulent model and transition model in CFD code ReFRESCO and compared the results with paint test data available for two kinds of propellers. Wang and Walters [21] predicted the performance of a model scale propeller P5168 with transition sensitive turbulence model in Loci/CHEM solver and found that this model is better able to resolve boundary surface stresses, flow separation and tip vortex origination. Recently Xu et al. [22] have investigated the capabilities of three different and non-isotropic low-Re turbulence closure models, including empirical transitional models, to predict natural or separation-induced

transition on 2D hydrofoils at low Reynolds numbers.

The focus of this paper is to address one of the potential reason for the discrepancy between experimental results and numerical results for low Reynolds number propeller. After validating the transitional turbulence model with experimental results for model scale propeller which operates at low Reynolds number, this study aims to investigate and evidence the substantial difference in the prediction of local and global hydrodynamic characteristics of low Reynolds number ducted propellers. The main theoretical aspects of the $\gamma - Re_\theta$ transition model are given in Section 2. The CFD model, its verification and validation for open propeller is discussed in Section 3. In-depth discussion and analysis of CFD simulations for ducted propeller are given in Section 4. Summary and conclusion are included in Section 5.

2. RANSE turbulence closure

In our present case, the fluid is considered incompressible and flow is assumed to be steady. The Reynolds-Averaged Navier-Stokes equation for incompressible Newtonian fluid is given below

$$\frac{\partial u_j}{\partial x_j} = 0 \quad (1)$$

$$\rho \left(\frac{\partial u_i}{\partial t} + u_j \frac{\partial u_i}{\partial x_j} \right) = - \frac{\partial P}{\partial x_i} + \mu \frac{\partial^2 u_i}{\partial x_j \partial x_j} - \frac{\partial u_i \bar{u}_j}{\partial x_j} \quad (2)$$

where ρ is the fluid density, μ is the dynamic viscosity and the $u_i \bar{u}_j'$ is the Reynolds stress term.

Using Boussinesq eddy viscosity assumption we can relate Reynolds stresses to mean strain rate S_{ij} by eddy viscosity μ_t as follows

$$u_i \bar{u}_j' = \frac{2}{3} k \delta_{ij} - 2\mu_t S_{ij}; \quad S_{ij} = \frac{1}{2} \left(\frac{\partial u_i}{\partial x_j} + \frac{\partial u_j}{\partial x_i} \right) \quad (3)$$

where k is the turbulent kinetic energy and δ_{ij} is Kronecker symbol.

The $\gamma - Re_\theta$ transition model proposed by Menter et al. [23] and applied by Langtry et al. [16] is an empirically derived correlation-based model that has been specifically formulated for unstructured CFD codes. This model is based on two additional transport equations, one for the intermittency γ and one for the transition onset momentum thickness Reynolds number $Re_{\theta t}$, coupled with SST $k - \omega$ turbulent model [24]. This transition model provides a semi-local approach to predict the onset of transition in turbulent boundary layer and it relies on calibration from experimental data. The transport equation for the intermittency is formulated as

$$\rho \frac{D\gamma}{Dt} = \nabla \cdot \left[\left(\mu + \frac{\mu_t}{\sigma_\gamma} \right) \nabla \gamma \right] + P_\gamma - E_\gamma \quad (4)$$

where P_γ and E_γ are the production and destruction terms given as

$$P_\gamma = F_{\text{Length}} C_{a1} \rho S [\gamma F_{\text{onset}}]^{1/2} (1 - C_{e1} \gamma) \quad (5)$$

$$E_\gamma = C_{a2}\rho W\gamma F_{turb}(C_{e2}\gamma - 1); \quad F_{turb} = \exp\left[-\left(\frac{Re_t}{4}\right)^4\right] \quad (6)$$

where C_{a1} , C_{e1} , C_{a2} , C_{e2} are model constants. The value of these constants are $C_{a1} = 0.5$, $C_{e1} = 1.0$, $C_{a2} = 0.03$, $C_{e2} = 50$. F_{Length} is an empirical correlation that controls the length of transition region and this correlation is suggested by Suluksnna et al. [25]. F_{onset} is a trigger function that describes the initiation of intermittency for different modes of transition. S and W are the modulus of mean strain-rate tensor and mean vorticity tensor respectively. F_{turb} is used to disable the destruction/relaminarization sources outside of a laminar layer or in the viscous sublayer and it is a function of turbulent Reynolds number Re_t .

The transport equation of the transition momentum thickness Reynolds number $\bar{Re}_{\theta t}$ is formulated as

$$\rho \frac{D \bar{Re}_{\theta t}}{Dt} = \nabla \cdot \left[\left(\mu + \frac{\mu_t}{\sigma_\gamma} \right) \nabla \bar{Re}_{\theta t} \right] + P_{\theta t} \quad (7)$$

where $P_{\theta t}$ is a source term designed to force the transported scalar $\bar{Re}_{\theta t}$ to match the local value of transition onset momentum thickness Reynolds number $Re_{\theta t}$ outside the boundary layer. The empirical relation for $Re_{\theta t}$ can be found in Langtry [26]. The transport equation for turbulent kinetic energy k used in SST $k - \omega$ is modified as below to be used in $\gamma - Re_\theta$ transition model

$$\frac{Dk}{Dt} = \nabla \cdot [(\mu + \sigma_k \mu_t) \nabla k] + \gamma P_k - \min[\max(\gamma, 0, 1), 1] D_k \quad (8)$$

where P_k and D_k are the production and destruction terms from the turbulent kinetic energy equation in the original SST $k - \omega$ turbulent model [24].

3. Model setup, verification and validation

The propeller considered in this study for validation is the propeller C from a study carried out by Kuiper [12]. Four propellers were studied for laminar to turbulent boundary layer transition at model scale in this study. Paint pattern data is available on the suction and pressure side of the surface of this propeller. In addition, the chord-wise location of laminar to turbulent flow transition on pressure and suction side of the propeller is available for two different loading conditions and two different Reynolds number. Also, the thrust and torque were measured for this propeller from advance ratio $J = 0$ to 1 at higher Reynolds number. The validated CFD model is then used for investigating ducted propeller K_a -4-70 inside the duct 19A. The accelerating duct 19A has $L/D = 0.5$ and is used for higher loading condition like bollard pull condition. The geometry of the propeller is available in the form of back and face coordinates at various radial location [27]. The gap between the propeller tip and the duct is 0.83% of the propeller radius. The geometrical details of both propellers are given in Table 1.

Both propellers are modeled with a front hubcap and downstream shaft following the open water setup with the full cylindrical fluid domain. The cylindrical domain extends 3D from the propeller plane to the inlet, 6D from propeller plane to the outlet and with a radius of $4D$, where D is the propeller diameter. The computational domain is divided into two regions, a stationary region, and a rotating region. In this study, steady-state Moving Reference Frame (MRF) approach is used because it requires less computation time as compared to unsteady

Table 1

Geometry of two propellers used in this study.

Parameter	Open propeller	Ducted propeller
Number of blades	4	4
Diameter (m)	0.3	0.24
A_E/A_O	0.63	0.7
$C_{0.7}/D$	0.43	0.36
$t/C(0.7)$	0.022	0.038

sliding mesh approach. The rotating domain extends 0.5D upstream from the propeller plane and 0.5D downstream from the propeller plane. Fig. 2 shows the geometry of ducted propeller and computational domain. The same computational domain was used for the open propeller also.

Table 2 gives the boundary conditions that were used for the CFD model. For open propeller, turbulent intensity is available from the experimental setup [28] and turbulent viscosity ratio is obtained by tuning inlet parameters for transition model (as discussed in Section 3.2.1). Both turbulent intensity and turbulent viscosity ratio are obtained by tuning inlet parameters based on hydrodynamic forces for the ducted propeller. The second-order upwind scheme is used for the discretization of momentum equation. For the turbulence model, the second-order upwind scheme is used.

3.1. Grid generation and mesh sensitivity analysis

The computational domain is discretized using unstructured polyhedral cells including the prism layers on the wall surface. The propeller has very small leading edge radius and a very small gap between the propeller tip and the duct. Hence, very fine meshing is needed in these regions to capture the flow correctly. To get accurate flow prediction in these regions, volumetric controls are created in the form of a cylinder which covers the leading edge and tip of each propeller blade. The interface between the rotating and stationary region has two prism layers on both sides for smooth movement of flow from one region to another. Fig. 3 shows various types of refinement zones created for the ducted propeller. Similar refinement zones were also created around the open propeller.

Table 3 gives the details of mesh parameters that were used to perform mesh sensitivity analysis. If the first cell layer height is used in different meshes, different wall functions will be used based on the value of $y+$ since we are using all- $y+$ treatment. In order to make sure that the same wall treatment is used for all three meshes, the first cell height is kept the same and is calculated in such a way that wall $y+ \approx 1$ is achieved on the surface of the propeller. The wall $y+ \approx 1$ ensures that no wall functions are used. The number of prism layer is systematically increased from coarse mesh to fine mesh to see the effect of growth ratio of cells in boundary layer on hydrodynamic coefficients. Fig. 4a–c shows the prism layer around the surface of open propeller at $\frac{r}{R} = 0.7$ for three meshes used. Fig. 4d–f shows the mesh on the propeller and the duct for three grid sizes used in this study. Figs. 5 and 6 shows the wall $y+$ on the surface of propeller blades for open and ducted propeller respectively. It can be observed that as the mesh becomes finer leading edge separation and trailing edge separation is better predicted. For mesh sensitivity analysis, the hydrodynamic coefficients are compared with experimental results at advance coefficient $J = 0.4$ and $J = 0.3$ for open and ducted propeller respectively. Hydrodynamic coefficients of the open and ducted propeller are calculated as below

$$K_{TP} = \frac{T_P}{\rho n^2 D^4}; \quad K_{TN} = \frac{T_N}{\rho n^2 D^4}; \quad K_Q = \frac{Q}{\rho n^2 D^5}; \quad K_T = K_{TP} + K_{TN}; \quad \eta = \frac{J}{2\pi} \frac{K_T}{K_Q}$$

where T_P , T_N , Q , J is the propeller thrust, duct thrust, propeller torque and advance coefficient respectively.

The results of mesh sensitivity analysis for open propeller are given in Fig. 7a. The forces predicted by all three meshes are almost the same and that might be due to the same first cell layer height in the prism layer. For different first cell layer height in different meshes, different wall functions will be used based on the value of $y+$ since we are using all- $y+$ treatment. In order to make sure that the same wall treatment is used for all three meshes, the first cell height is kept the same. The relative error between experimental torque coefficient and CFD torque

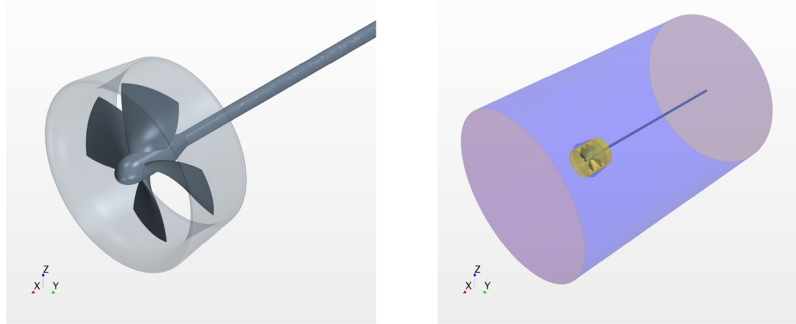


Fig. 2. Geometry of the propeller K_a -4-70 inside the duct 19A (left). Computational domain used for CFD simulations (right).

Table 2
Boundary conditions for CFD calculations.

Boundary	Velocity	Pressure	Turbulent intensity	Turbulent viscosity ratio
Inlet	Constant (based on value of J)	$\frac{\partial P}{\partial n} = 0$	3% (open), 1% (ducted)	30 (open), 10 (ducted)
Outlet	$\frac{\partial V}{\partial n} = 0$	Ambient pressure	1%	10
Cylinder surface	$\frac{\partial V}{\partial n} = 0$	$\frac{\partial P}{\partial n} = 0$	Wall function	Wall function
Propeller, duct, hub, shaft	No slip	$\frac{\partial P}{\partial n} = 0$	Wall function	Wall function
Rotating/stationary region interface	Internal interface	Internal interface	Internal interface	Internal interface

coefficient reduces from 1.45% to 1.27% from coarse mesh to fine mesh. The results for ducted propeller are presented in Fig. 7b. The relative error of torque coefficient reduces from 0.82% to 0.77% from coarse mesh to fine mesh. In the case of thrust coefficient, all meshes overpredict the thrust and the relative error changes from 1.69% to 1.95% from coarse mesh to fine mesh. No monotonic convergence is found, but it is believed that the experimental measurement uncertainty is in the same order of magnitude of the deviation of the numerical prediction error.

3.2. Validation study for open propeller

In this section, the validation of the CFD model for an open propeller with the experimental results found by Kuiper [12] is presented. The local characteristics such as the location of laminar to turbulent transition and global characteristics like hydrodynamic forces are compared between the CFD simulation results and experimental results.

3.2.1. Influence of turbulence inlet parameters

The $\gamma - Re_\theta$ transition model takes into account the effect of free-stream turbulence levels on the transition location. Hence, the special attention should be given to the inlet turbulence parameters when using the transition model. Since the inlet boundary is located at $4D$ upstream from the propeller plane, there is a decay of turbulent kinetic energy

from the inlet boundary to the propeller region. The decay in turbulent intensity and turbulent viscosity ratio from the inlet to the propeller plane is given by below equations.

$$I = I_{inlet} \left[1 + \frac{0.1242x\rho U_\infty I_{inlet}^2}{\mu TVR_{inlet}} \right]^{-0.5435} \quad (9)$$

$$TVR = TVR_{inlet} \left[1 + \frac{0.1242x\rho U_\infty I_{inlet}^2}{\mu TVR_{inlet}} \right]^{-0.087} \quad (10)$$

where x is the distance in streamwise direction from inlet plane, I_{inlet} is turbulent intensity at the inlet, TVR_{inlet} is the turbulent viscosity ratio at the inlet and U_∞ is the freestream velocity.

The higher value of turbulent viscosity ratio will reduce the decay in turbulent intensity significantly. However, a rough guideline is that the turbulent viscosity ratio should be lower than the turbulent viscosity occurring within the boundary layer. In order to have the same turbulent kinetic energy in the propeller region as the inlet boundary, additional source term is added in the turbulent kinetic energy transport equation. An ambient source option in StarCCM+ keeps the turbulence intensity constant over the domain. For the experimental setup, there was 3% disturbance in the velocity in the upstream region of the propeller [28]. Hence, the turbulent intensity is kept constant at $TI = 3\%$ and three values of turbulent viscosity ratio are considered: $TVR = 10, 30$ and 100 . Fig. 8 shows the skin friction coefficient contour

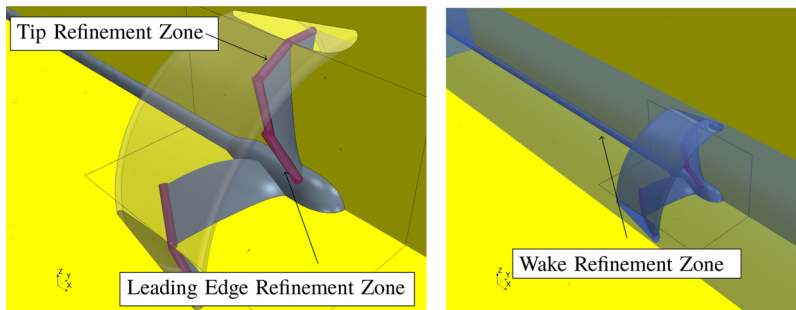


Fig. 3. Various mesh refinement zones created in computational domain around the propeller's leading edge and the tip.

Table 3

Mesh parameters used for mesh sensitivity study.

	Fine	Medium	Coarse
Cell type	Polyhedral	Polyhedral	Polyhedral
Target surface mesh size – Propeller	0.25% D	0.3125% D	0.375% D
Target surface mesh size – Duct	0.67% D	0.84% D	1% D
Surface mesh size – LE and tip volume	0.17% D	0.21% D	0.25% D
Surface mesh size – Rotating region	3.3% D	4.1% D	5% D
Prism layer thickness	3.2 mm (ducted), 2.5 mm (open)	3.2 mm (ducted), 2.5 mm (open)	3.2 mm (ducted), 2.5 mm (open)
Number of prism layers	25	20	15
Maximum wall Y +	25	20	15
Cell count	24.7 M (ducted), 28.3 M (open)	13.7 M (ducted), 15.7 M (open)	8.5 M (ducted), 11.8 M (open)

on the suction and pressure side of the propeller for different values of turbulent viscosity ratio at 60% slip. The slip is defined as the ratio of the difference between theoretical travel (pn) and actual travel (V_a) to theoretical travel. The skin friction coefficient is calculated using an effective velocity $V_E = \sqrt{V_A^2 + (2\pi n r)^2}$ at each radial location. The skin friction coefficient magnitude on the surface of propeller results in a range of values that lies in laminar to turbulent transition region friction coefficient for the flat plate at given Reynolds number. The extent of the turbulent region on the surface of the propeller increases with an increase in turbulent viscosity ratio.

Fig. 9a shows the location of transition for different values of TVR for 60% slip and chord-based Reynolds number of $0.665 \cdot 10^6$. The Reynolds number is based on $r/R = 0.7$ location. It can be clearly seen that the location of transition shifts toward leading edge with an increase in TVR. The results are in good agreement with the experimental results for $TVR = 30$. The CFD results for the position of transition are further compared for two Reynolds number and two loading conditions. **Fig. 9b** shows the comparison of chord-wise position of transition at $r/R = 0.7$. The transition model predicts the transition position correctly for 30% slip which is a light loading condition. At higher loading condition of 60% slip, the transition model predicts earlier transition to turbulent flow than the experimental results.

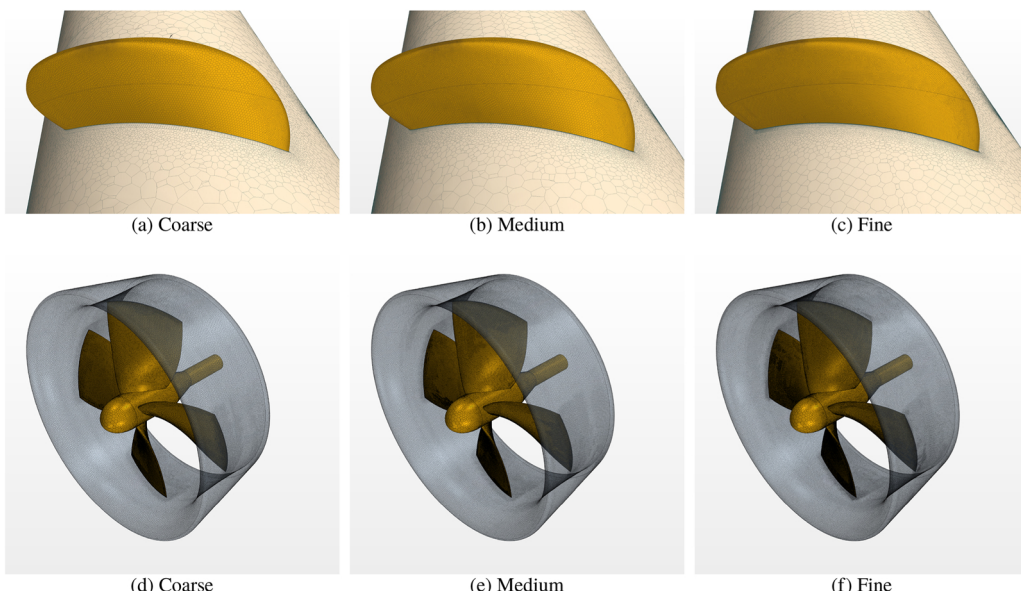
3.2.2. Paint pattern visualization

In this section paint pattern is compared for open propeller at 30% slip and $Re_N = 0.66 \cdot 10^6$ where $Re_N = nD^2/\nu$. The streamline pattern on the surface of propeller gives an indication of the relative strength of the centrifugal force and tangential force. Tangential forces are due to

friction between the fluid and the propeller. Based on the laminar or turbulent region, the frictional forces vary and hence the direction of streamlines changes depending upon the dominant force. Hence, if streamlines are directed in the radial direction then the centrifugal forces are dominant and hence the flow is in the laminar region. If the streamlines are directed in the tangential direction, then tangential forces are dominant and hence the flow is in the turbulent region. In addition, the skin friction coefficient is higher in case of turbulent flow than for the laminar flow. Therefore skin friction coefficient increases as flow changes from laminar to turbulent flow.

The results of the paint test on the propeller surface are compared with the constrained streamlines for wall shear stress predicted by transition and fully turbulent model for open propeller. **Fig. 10** shows that there is a good qualitative agreement is obtained between the paint test and the transition model results. The transition model is able to predict the change in orientation of streamlines due to transition. The transition model predicts larger turbulent region especially on the pressure side as compared to the experimental results. The streamline direction matches with the paint pattern in the region near the hub up to $r/R = 0.5$. In the outer region there is an earlier transition to turbulent flow as compared to experimental results on both suction and pressure side. The fully turbulent model on the other hand does not predict the direction of streamlines correctly. The streamlines are directed in the tangential direction on whole surface of the propeller for fully turbulent model.

The contribution of pressure and shear resistance forces calculated by transition and turbulent model is given in **Table 4**. The shear force predicted by the transition model is around 13% less than the fully turbulent model. A decrease in skin friction leads to slight increase in

**Fig. 4.** Particulars of the mesh scenes for open and ducted propeller.

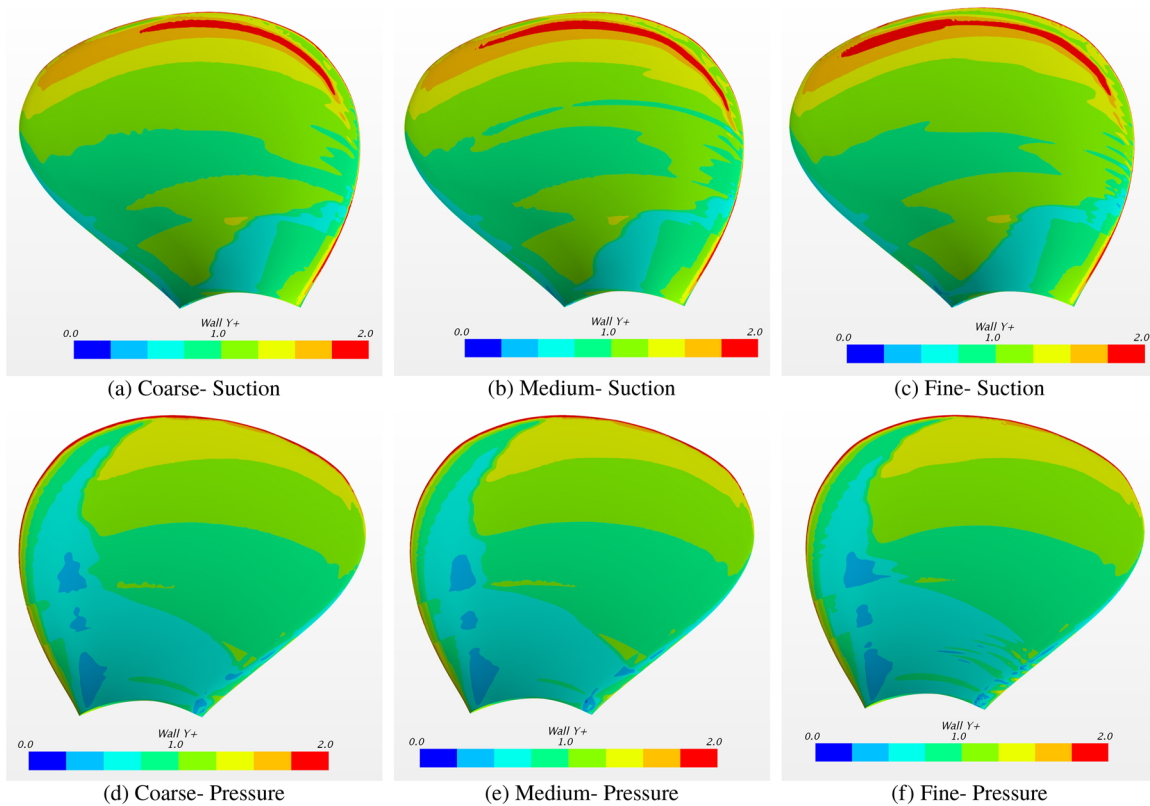


Fig. 5. Wall Y^+ on the surface of open propeller for different meshes used at $J = 0.3$.

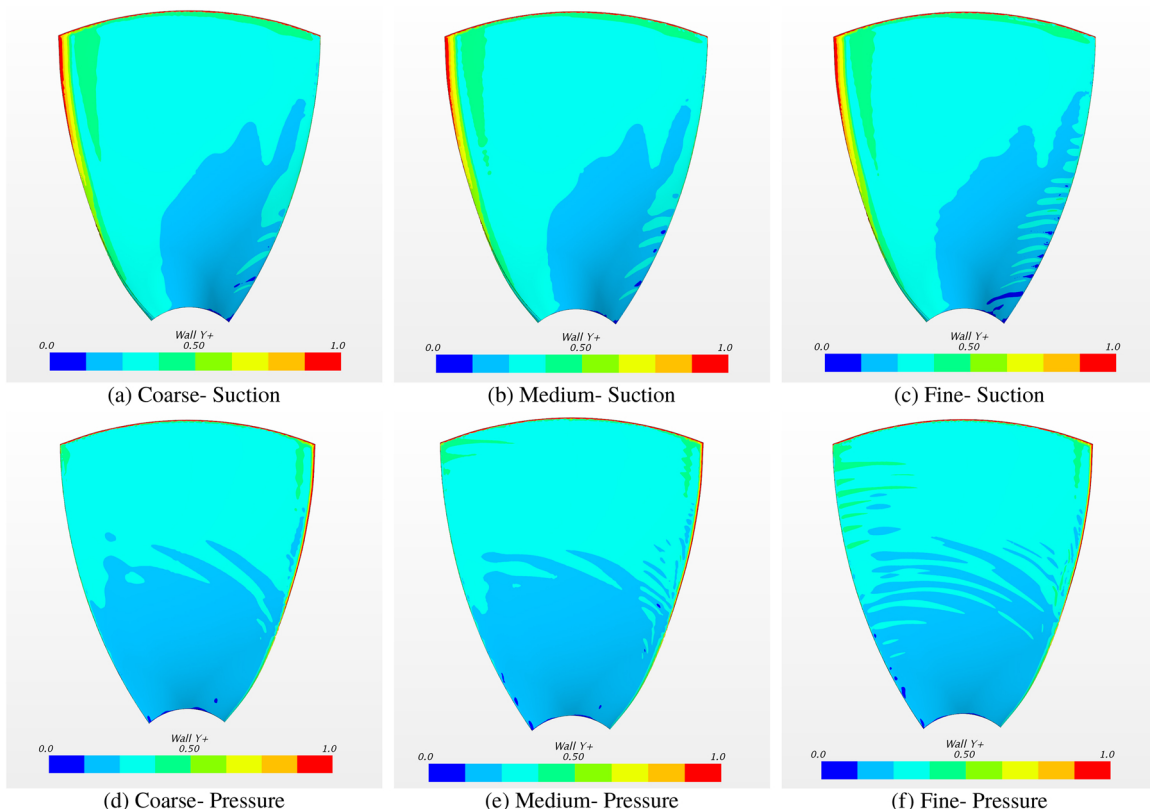


Fig. 6. Wall Y^+ on the surface of propeller K_a -4-70 inside the duct for different meshes used at $J = 0.4$.

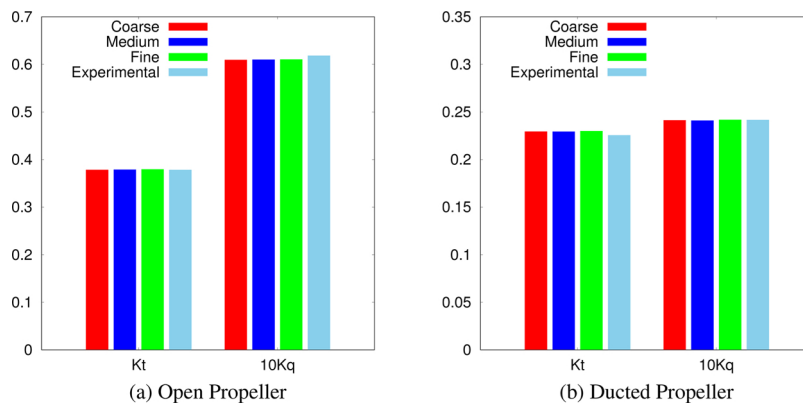


Fig. 7. Mesh sensitivity analysis results for open propeller at $J = 0.4$ and for ducted propeller at $J = 0.3$.

thrust predicted by the transition model. The overall torque calculated by both transition and fully turbulent model is almost same due to higher contribution of pressure force compared to shear force.

3.2.3. Open water performance comparison

In this section open-water performance is presented for the open propeller. The results are compared with experimental data obtained by Kuiper [12] for propeller C. The open-water forces were calculated at $Re_N = 2.9E6$ and same rotational speed of the propeller is used for CFD simulations. The magnitude of inlet velocity is calculated based on advance coefficient. For open-water performance calculation same turbulent inlet parameters ($Tu = 3\%$ and $TVR = 30$) are used at all advance coefficient. For all the force and moment measurement, both pressure and viscous forces are integrated over the surface of the propeller blades.

The comparison of the thrust and torque coefficient calculated using transition model and experimental results are presented in Fig. 11a. The difference between numerical results and experimental results for thrust and torque coefficient is within 5% up to advance coefficient $J = 0.7$. The thrust predicted by CFD simulation is up to 15% less than the experimental results at advance coefficients higher than $J = 0.7$. At $J = 1.0$ the thrust of the propeller is near zero value and the absolute error between the numerical and experimental results is small. At these advance coefficients, the torque coefficient is up to 8% lower than the experimental results. This shows that the transition model is able to capture the boundary layer transition correctly at all advance coefficients. The efficiency calculated using CFD simulation is within 7% at all advance coefficient.

The open-water performance of the open propeller is further calculated using fully turbulent ($SST k - \omega$) model. The results for

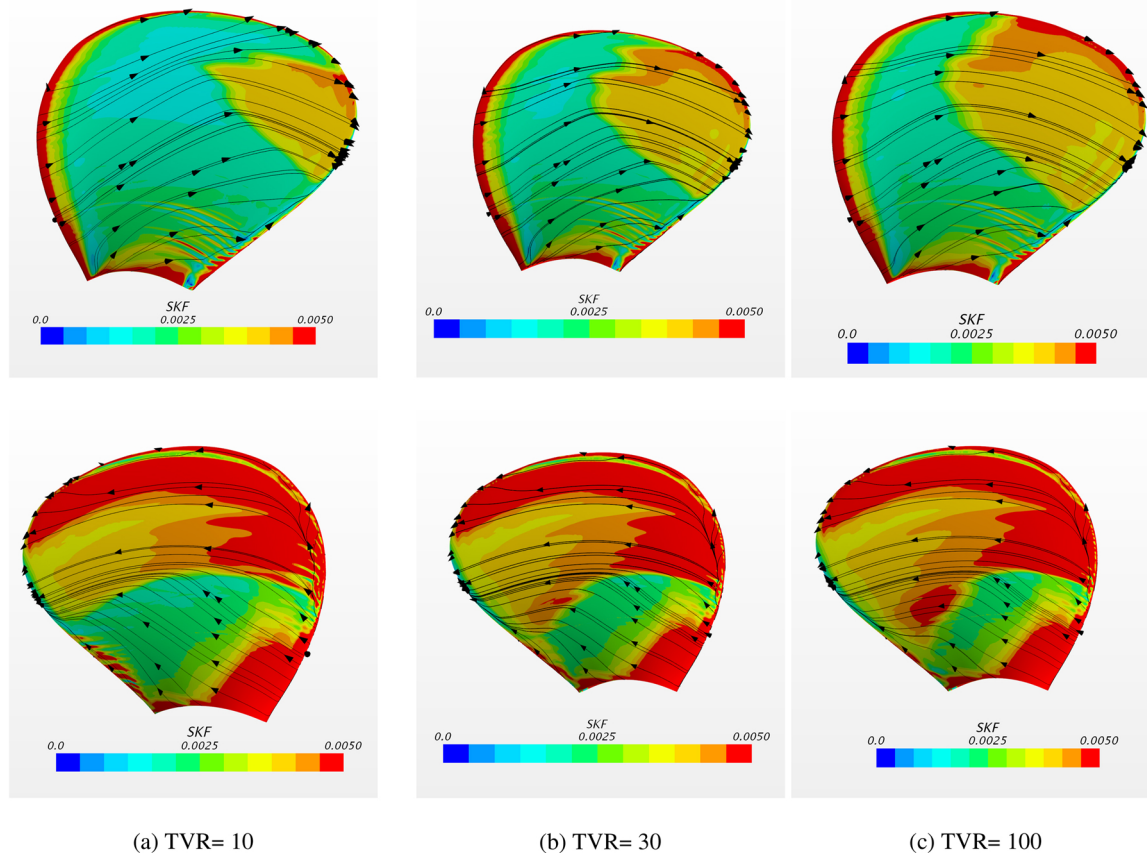


Fig. 8. Skin friction coefficient contour for $TI = 3\%$ and different values of turbulent viscosity ratio at 60% slip. Top: pressure side; bottom: suction side.

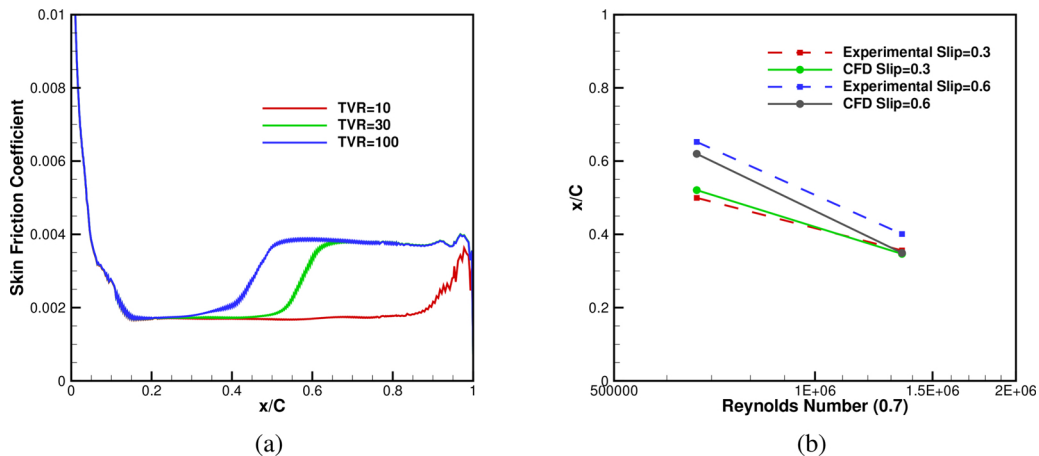


Fig. 9. Comparison of CFD results for chord-wise position of transition with experimental results [12]. Left figure is for 60% slip and $Re = 0.66 \cdot 10^6$.

transition and fully turbulent model is shown in Fig. 11b. The forces predicted by both model are almost same at all advance coefficients. This may be due to the higher Reynolds number $Re_N = 2.9E6$ at which open-water performance data was measured.

4. Results for ducted propeller

In this section, local and global hydrodynamic characteristics are presented for propeller K_a -4-70 with P/D = 0.8 inside the duct 19A. The geometrical details of this propeller are given in Table 1. The speed of rotation of this propeller was kept constant at $n = 6.3$ rps for open-water performance measurement. The Reynolds number of flow on the surface of propeller ranges from $1.4 \cdot 10^5$ to $4.7 \cdot 10^5$. At this Reynolds number, the flow is in the transitional region on the surface of the propeller.

4.1. Influence of turbulence inlet parameters

As discussed in case of the open propeller (Section 3.2.1), the $\gamma - Re_\theta$ transition model results strongly depend upon the turbulent

Table 4

Contribution of pressure and shear forces for thrust and torque of the propeller at slip = 0.3 and $Re_N = 0.66E6$.

Type	Turbulent model		Transition model	
	Thrust (N)	Torque (N-m)	Thrust (N)	Torque (N-m)
Pressure	88.004	4.249	90.033	4.346
Shear	-2.776	0.549	-2.430	0.479
Total	85.228	4.798	87.603	4.825

inlet parameters. Hence different values of turbulent intensity and turbulent viscosity ratio are used and its influence on hydrodynamic coefficients is considered. For all the turbulent inlet parameters, the ambient source option was used which keeps the turbulent intensity constant over the domain as the inlet boundary. In all these cases, the advance coefficient was kept constant at $J = 0.5$.

For the propeller K_a -4-70 the paint pattern data is not available and hence we cannot compare the constrained streamlines on the surface of the propeller. We can compare hydrodynamic coefficients for different

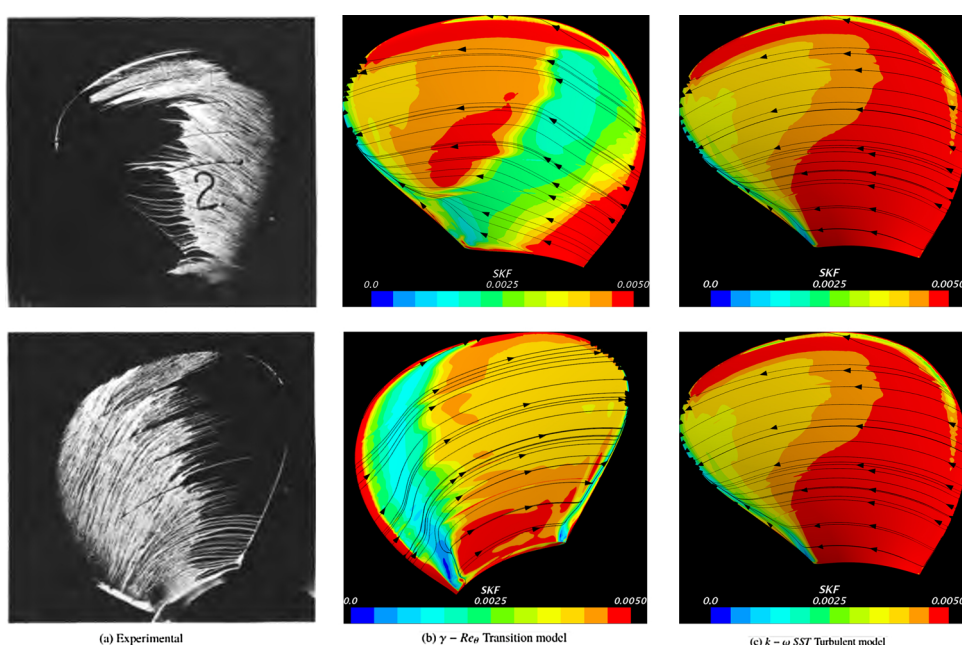


Fig. 10. Comparison of constrained streamline with skin friction coefficient on the surface of propeller blade with experimental results for paint pattern test [12] at 30% slip and $Re_N = 0.66 \cdot 10^6$. Top: suction; bottom: pressure.

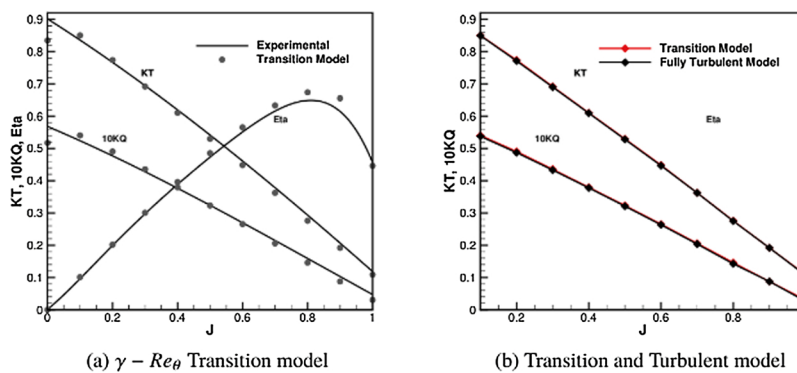


Fig. 11. Open-water performance comparison for open propeller calculated using RANSE solver with transition model and experimental results [12] (left). Comparison of hydrodynamic coefficients for fully turbulent and transition model (right). All forces were measured at $Re_N = 2.9E6$.

Table 5

Effect of turbulence inlet parameters on hydrodynamic coefficients at $J = 0.5$ for ducted propeller.

Turbulent intensity	Turbulent viscosity ratio	K_{TN}	K_{TP}	K_T	$10K_Q$
Experimental results					
1%	10	0.0072	0.1094	0.1166	0.1864
3%	10	0.0148	0.1164	0.1312	0.1916
5%	10	0.0173	0.1171	0.1344	0.2010
5%	100	0.0179	0.1178	0.1358	0.2078
		0.0174	0.1176	0.1349	0.2119

turbulent inlet parameters to find the correct parameters for the transition model. The hydrodynamic coefficients for different turbulence inlet parameter are given in Table 5. It can be seen that the thrust of the propeller and the duct is not influenced by turbulent inlet parameters as compared to the torque coefficient.

As the turbulent intensity increases, we see that the torque coefficient also increases. The shear stress is higher for turbulent flow than the laminar flow. As the torque of the propeller depends upon the shear stress, a higher value of torque suggests that the boundary layer on the surface of the propeller is mainly turbulent. At model scale, the flow on the surface of the propeller is in transition regime and hence the turbulent inlet parameters ($I = 1\%$ and $TVR = 10$) are suitable for the transition model.

4.2. Open water performance comparison

In this section open-water performance is presented for the ducted propeller. The results are compared with experimental data obtained by Oosterveld [27] for propeller K_a -4-70 with $P/D = 0.8$. For all advance coefficients, the speed of rotation of the propeller was kept constant at $n = 6.3$ rps and inlet velocity is changed to get the required value of J . For open-water performance calculation same turbulent inlet parameters ($I = 1\%$ and $TVR = 10$) are used at all advance coefficient. Both pressure and viscous forces are integrated over the surface of the propeller blades for force and moment calculation.

The comparison of the thrust and torque coefficient calculated using CFD simulation and experimental results are presented in Fig. 12a for transition model. The hydrodynamic coefficients calculated using transition model and fully turbulent model are compared in 12 b. The total thrust coefficient is within 5% at all advance coefficients except for at $J = 0.5$ for both fully turbulent and transition model. The torque coefficient is within 4% at all advance coefficient for the transition model. However, the fully turbulent model overpredicts the torque coefficient by more than 5% at all advance coefficients (as seen in Fig. 12b). This suggests that the transition model is able to capture the correct boundary layer on the surface of the propeller than the fully turbulent model. The difference between the experimental and

numerical results for duct thrust is larger at higher advance coefficient. At higher advance coefficient the duct thrust is very small and the absolute error between CFD results and experiment is very small. Baltazar et al. [29] made similar observations for the duct thrust at higher advance ratios.

4.3. Flow pattern on the propeller

In order to understand the difference in torque coefficient predicted by turbulent and transition model in Section 4.2, the constrained streamline pattern with skin friction coefficient is compared for both transition and fully turbulent model at three different loading conditions.

Figs. 13 and 14 shows the constrained streamline pattern on pressure and suction side of the propeller for three loading conditions respectively. It can be clearly seen that the skin friction coefficient predicted using fully turbulent model is higher than the transition model at all loading conditions. The constrained streamline pattern is in tangential direction over the surface of the propeller for the fully turbulent model. The transition model predicts the constrained streamlines in a radial direction indicating that the flow is in the laminar-turbulent transition region and centrifugal forces are significant in comparison to tangential shear stress. The transition model predicts trailing edge separation which is not predicted by the fully turbulent model.

The contribution of pressure and shear resistance forces calculated by transition and turbulent model is given in Table 6 at advance coefficient $J = 0.3$. The shear force predicted by the transition model is around 45% less than the fully turbulent model. A decrease in skin friction leads to slight increase in thrust predicted by the transition model. The overall torque calculated by both transition and fully turbulent model is different due to over-prediction of shear force by fully turbulent model.

4.4. Flow field around the duct

The relative contribution to total thrust from the duct increases with an increase in propeller loading. As the propeller loading changes the flow field around the duct also changes. Fig. 15 shows the line integral convolution streamline of the velocity field around the duct at different advance coefficients.

It can be clearly seen that the stagnation point position changes with the change in propeller loading. At advance coefficient $J = 0.1$, the stagnation point is on the outer surface of the duct and with an increase in the advance coefficient, the stagnation point shifts towards the leading edge of the duct. At advance coefficient $J = 0.4$, the flow almost approaches along the camber line of the duct. The stagnation point then shifts slightly towards the inner surface of the duct for higher advance coefficients of $J = 0.5$ and 0.6 .

The flow starts separating at the leading edge of the duct and the

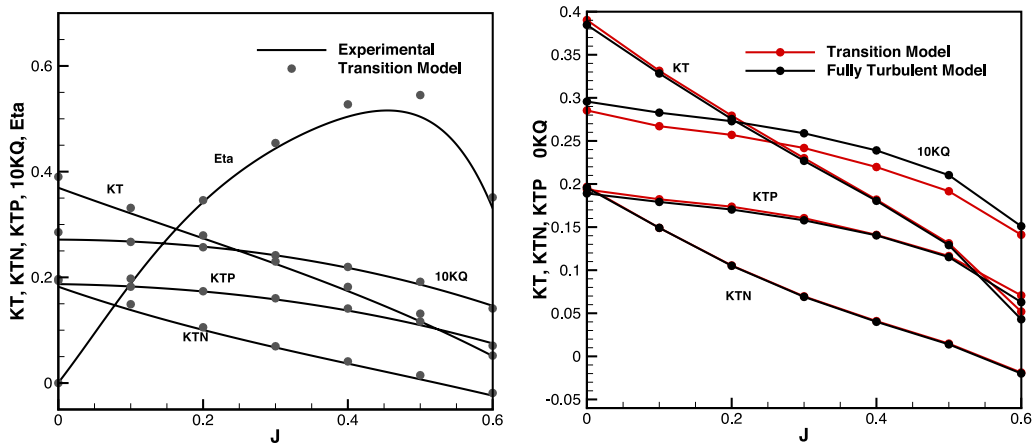


Fig. 12. Open-water performance comparison for ducted propeller K_a -4-70 with $P/D = 0.8$ inside the duct 19A for transition model (left) and experimental results [27]. Comparison of hydrodynamic coefficients for fully turbulent and transition model (right).

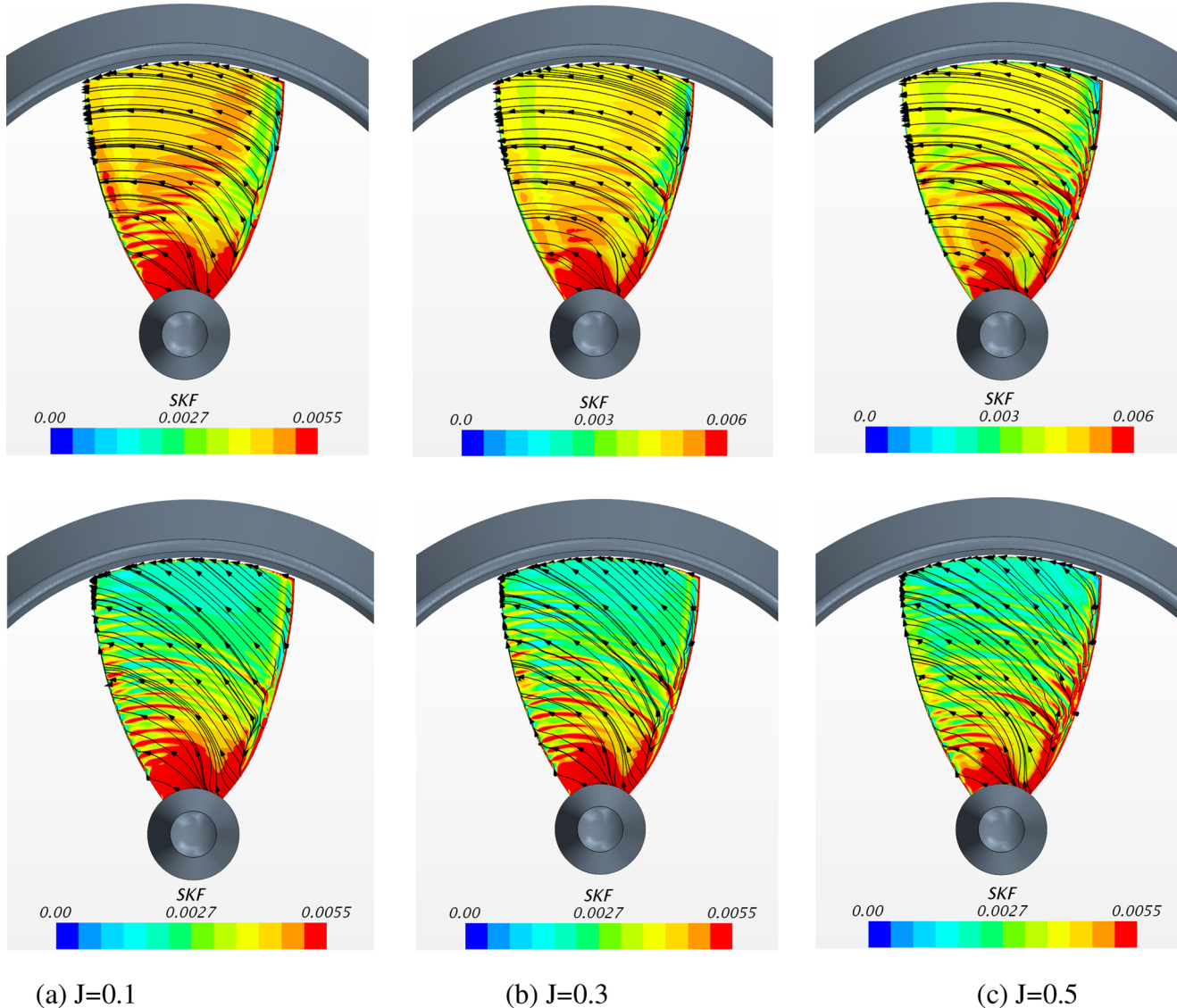


Fig. 13. Flow pattern on the pressure side of the propeller's surface for different loading conditions. Top: fully turbulent model; bottom: transition model.

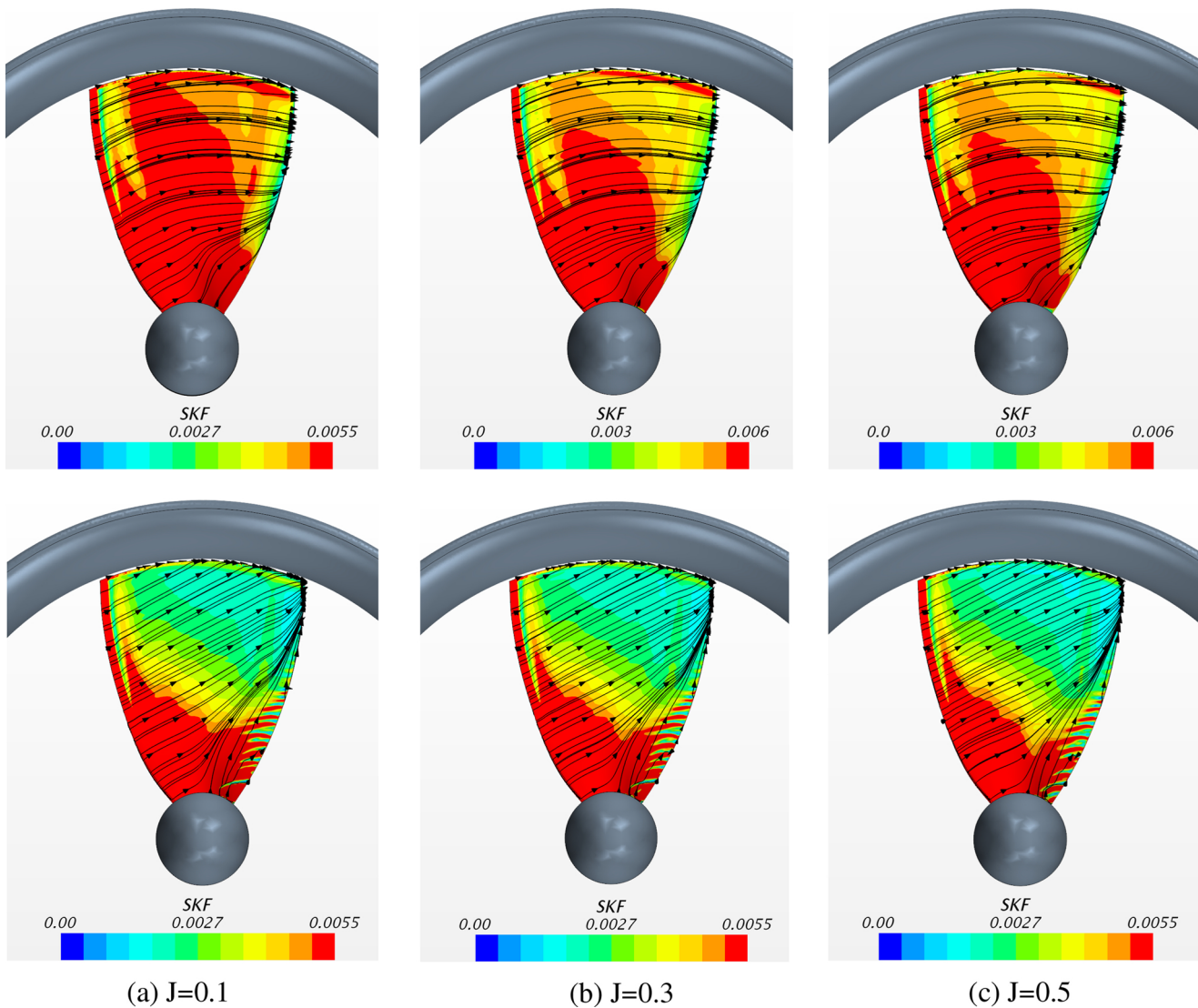


Fig. 14. Flow pattern on the suction side of the propeller's surface for different loading conditions. Top: fully turbulent model; bottom: transition model.

Table 6
Contribution of pressure and shear forces for thrust and torque of the ducted propeller at advance coefficient $J = 0.3$.

Type	Turbulent model		Transition model	
	Thrust (N)	Torque (N-m)	Thrust (N)	Torque (N-m)
Pressure	21.338	0.685	21.433	0.6915
Shear	-0.5221	0.1332	-0.304	0.0728
Total	20.816	0.818	21.129	0.764

separation bubble is predicted with the consequent transition at the reattachment point for advance coefficient $J = 0.5$. Bhattacharyya et al. [14] also found the separation bubble near the leading edge on the outer surface of the duct 19A with controllable pitch propeller inside the duct at advance coefficient $J = 0.6$. The reattachment point moves aft as the advance coefficient increases until it fully separates at $J = 0.6$. This shows that the propeller loading and type of propeller can have an effect on the flow separation on the outer surface of the duct. This confirms that the duct 19A is not suitable for low loading conditions (high advance ratios) for low Reynolds number propeller also. Since the duct has a blunt trailing edge, a pair of counter-rotating vortices is formed due to boundary layer separation from inner and

outer surface of the duct.

4.5. Tip gap flow analysis

The characteristic strong tip vortex flow which establishes on the propeller, due to the pressure difference between face and back, is substantially prevented by the presence of the duct. This flow in the tip gap is also influenced by the boundary layer on the inner side of the duct and the propeller tip, and the centrifugal force. Bhattacharyya et al. [14] showed that the separation on the inner side of the duct gets influenced by the tip vortex formed near the tip of the skewed propeller and it can modify the wake flow field and duct thrust. The propeller K_a -4-70 has a wide tip and hence accurate resolution of tip vortex is very important and can lead to improved prediction of duct thrust.

Fig. 16 shows the pressure coefficient for three advance coefficients on seven sections across the tip of the propeller at different chord position. The pressure coefficient is non-dimensionalized using resultant velocity from advance speed and rotational velocity of the tip. It can be seen that the tip vortex is formed and the flow gets attached to the suction side of the propeller blade. The size of the tip vortex formed increases from leading edge to the trailing edge at particular advance coefficient. With the change in the size of tip vortex, the attachment point on the suction side also changes. The size of the tip-vortex reduces

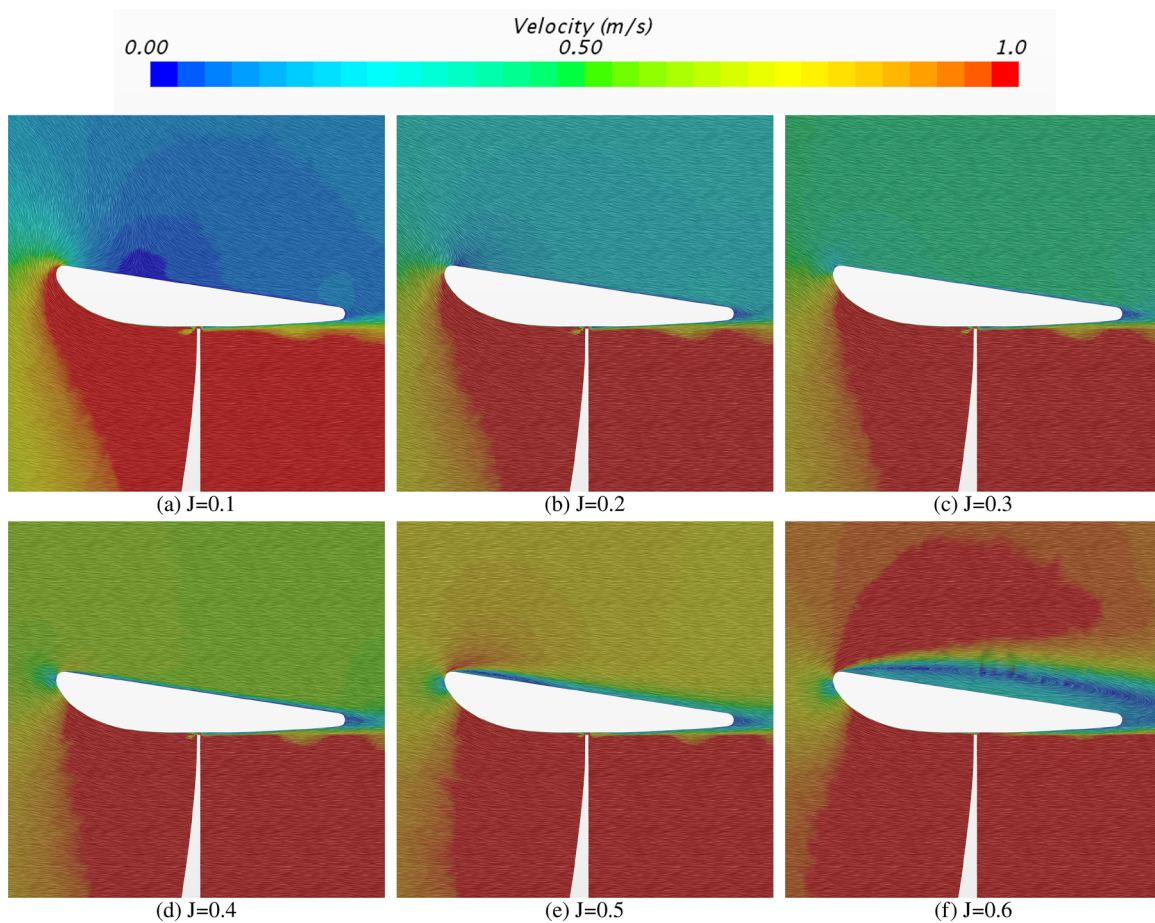


Fig. 15. Line integral convolution streamlines and velocity distribution around the duct for various advance ratios.

as the advance coefficient increases.

4.6. MRF and sliding mesh for propeller

In this section, we discuss the unsteady sliding mesh approach for modeling flow around the propeller. The analysis is done at advance coefficient $J = 0.5$ and results are compared with steady-state MRF

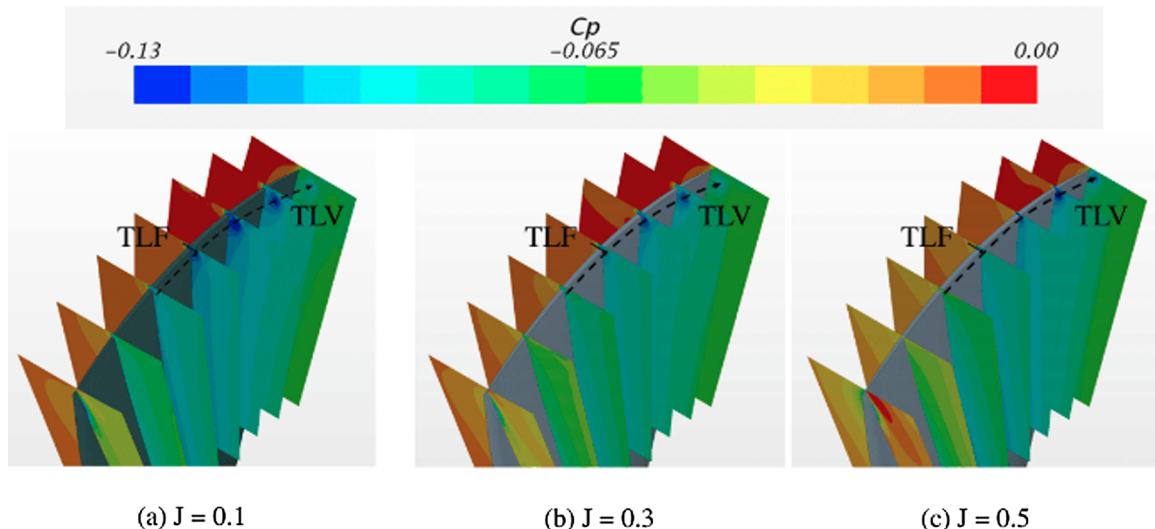


Fig. 16. TLF (tip leakage flow) and TLV (tip leakage vortex) with pressure coefficient contour at different chord location at the tip of the propeller for three loading conditions.

Table 7Hydrodynamic coefficient for MRF and sliding mesh approach for ducted propeller at $J = 0.5$.

Hydrodynamic coefficient	MRF	Sliding mesh	Experimental	Percentage error (MRF)	Percentage error (sliding mesh)
K_{TP}	0.1164	0.1176	0.1094	6.4	7.5
K_{TN}	0.0148	0.0176	0.0072	–	–
K_T	0.1312	0.1352	0.1166	12.5	15.9
$10K_Q$	0.1916	0.1963	0.1864	2.8	5.3

around 10 for few cells in prism layer near leading edge of the tip region. Table 7 gives the hydrodynamic coefficient calculated using both MRF and sliding mesh approach. The hydrodynamic coefficient predicted using MRF approach are in better agreement with the experimental results than the sliding mesh approach. The percentage error for duct thrust coefficient is very large due to small magnitude of duct thrust at advance coefficient $J = 0.5$.

In order to find the cause of the discrepancy between MRF and sliding mesh results, the flow field around the duct and tip leakage flow are compared for both approaches. Fig. 17 shows the flow field around the duct for two approaches. It can be seen that the MRF approach predicts a single separation bubble near the leading edge and on the outer surface of the duct. On the other hand, the sliding mesh approach predicts a separation bubbles smaller in size than predicted by MRF approach, in the same region. Also trailing edge vortex predicted using the sliding mesh approach is smaller than the one predicted by MRF approach.

Fig. 18 shows the tip leakage vortex predicted using MRF and sliding mesh approach at advance coefficient $J = 0.5$. The magnitude of pressure coefficient between the propeller tip and the inner surface of the duct is considerably different for both approaches. The pressure coefficient magnitude in the gap is lower in case of sliding mesh approach than the MRF approach. Hence the leakage flow from the pressure side to suction side is smaller for the sliding mesh approach and the total thrust predicted is higher as compared to the MRF approach. The difference in forces predicted by two approaches might be due to unsteady simulation and difference in the interpolation of flow quantities for sliding interface in case of sliding mesh approach. The velocity is exactly matched at the interface in case of MRF approach via the velocity transformation from one reference frame to another. Due to the lack of physical data it is difficult to say which approach is better and accurately predicts the flow around the ducted propeller.

5. Conclusion

Capabilities of a RANSE solver with $\gamma - Re_\theta$ transition model in StarCCM+ have been tested to investigate hydrodynamic

characteristics of the open and ducted propeller at low Reynolds number. The flow on the surface of the propeller is typically in transitional flow regime for sectional Reynolds number at $r/R = 0.7$ less than $1 \cdot 10^6$ [28] and the $\gamma - Re_\theta$ transition model can predict the flow accurately at these low Reynolds number. The results of mesh sensitivity analysis show that the wall $y+ = 1$ and finer grid resolution is important to capture details of flow field that are smoothed out by coarse grid resolution even if the predicted forces do not change significantly. Fine grid resolution can capture leading edge separation, laminar-turbulent transition and trailing edge separation correctly than the coarse mesh.

Low Reynolds number physics predicted by RANSE solver significantly change if the transition model is used instead of more conventional $k - \omega$ SST turbulent model. The transition model is validated using the location of the laminar-turbulent transition point for two loading conditions at two different Reynolds number for the open propeller. The results are also compared with paint pattern visualization data and constrained streamlines calculated using RANSE solver with the transition model. The constrained streamline on the surface of the propeller predicted by the transition model shows that the flow gets influenced by both centrifugal force and tangential shear stress. The transition model is sensitive to turbulence inlet parameters and hence inlet parameters should be tuned to get a correct prediction of different flow regimes on the surface of the propeller. Hence, better information about the paint pattern on the surface of the propeller or experimental measurement of turbulent intensity is needed to complement the transition model. The open-water performance calculated using the transition model is in good quantitative agreement with experimental results especially at the design and high loading condition.

The transition model is used for investigating flow around ducted propeller K_a -4-70 with $P/D = 0.8$ inside the duct 19A. The influence of turbulence inlet parameters on hydrodynamic coefficient shows that the forces and moment predicted by the CFD model are in good agreement with experimental results for $I = 1\%$ and $TVR = 10$. The transition model calculates hydrodynamic coefficients close to experimental results than the fully turbulent model. The difference between CFD results and experimental results for hydrodynamic coefficients are

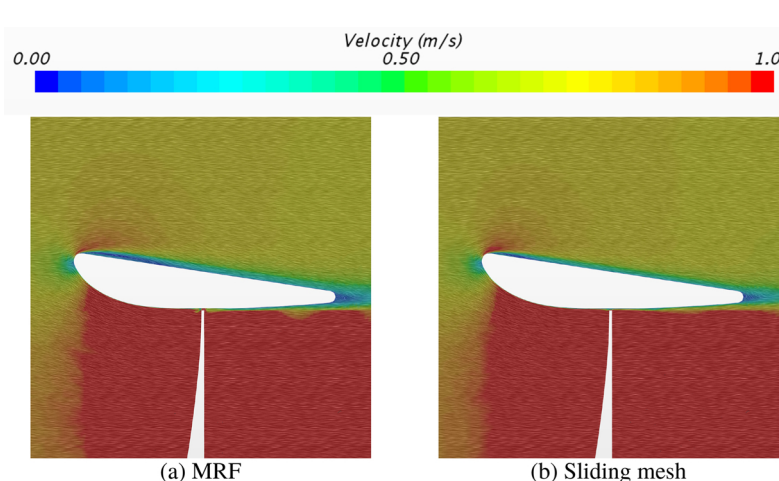


Fig. 17. Comparison of flow analysis around the duct at $J = 0.5$ for MRF and sliding mesh approach.

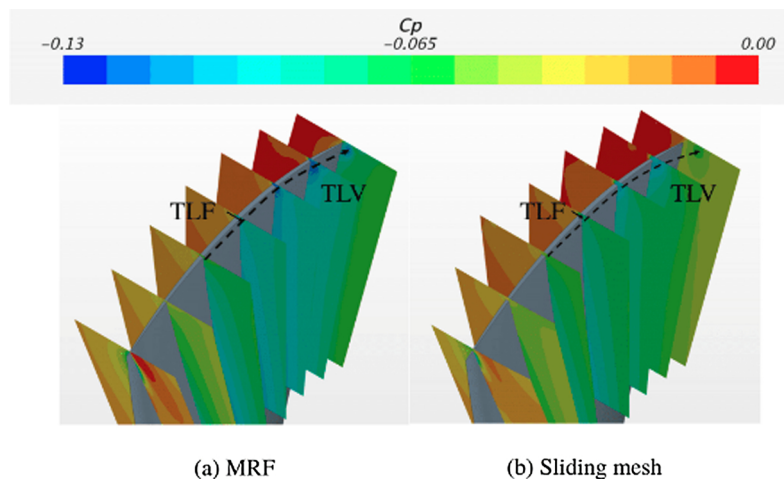


Fig. 18. TLF (tip leakage flow) and TLV (tip leakage vortex) with pressure coefficient contour at different chord location at the tip of the propeller at $J = 0.5$ for MRF and sliding mesh approach.

within 5% at all advance coefficient except for higher advance coefficient $J = 0.5$ for transition model. The constrained streamlines on the surface of the ducted propeller are almost in the radial direction indicating that centrifugal forces are dominant than the tangential shear stress.

The detailed analysis of the flow around the duct is presented for all advance coefficients. At lower advance coefficient, the stagnation point appears on the outer surface of the duct. The flow starts separating and separation bubble is found on the outer surface of the duct at a higher advance coefficient. As well known, it is confirmed that the duct 19A is not suitable for operating at higher advance coefficients even for propeller operating at low Reynolds number. The analysis of tip vortex at different loading conditions show that the size of tip leakage vortex reduces with an increase in advance coefficient due to a reduction in the pressure difference between two sides of the propeller. Finally, we model the ducted propeller using unsteady sliding mesh approach. The results for steady-state MRF approach are more consistent with experimental results than the unsteady sliding mesh approach. The overall conclusion of this paper demonstrates that the use of $\gamma - Re_{\theta}$ transition model can lead to accurate prediction of global and local hydrodynamic characteristics of open and ducted propeller at low Reynolds number.

Acknowledgements

This work has been possible thanks to the partial support of the Office of Naval Research, under grant N00014-16-1-2589. The authors wish to thank the program manager Reginald Beach. The authors would like to thank anonymous reviewers for reviewing this work and giving feedback which helped improve the quality of this paper.

References

- [1] A.B. Phillips, S.R. Turnock, M. Furlong, Comparisons of CFD simulations and in-service data for the self propelled performance of an autonomous underwater vehicle, 27th Symposium on Naval Hydrodynamics (2008).
- [2] S. Pyo, Numerical Modeling of Propeller Tip Flows with Wake Sheet Roll-up in Three Dimensions. Technical report, Massachusetts Inst. of Tech, Cambridge, Dept. of Ocean Engineering, 1995.
- [3] S. Gaggero, S. Brizzolara, Exact modeling of trailing vorticity in panel method for marine propeller, Proceedings of ICMRT (2007).
- [4] Y. Tian, S.A. Kinnas, A viscous vorticity method for propeller tip flows and leading edge vortex, 4th Symposium on Marine Propulsors, SMP, volume 15 (2015).
- [5] J.M. Baltazar, D. Rijkem, J.F. de Campos, J. Bosschers, Prediction of the open-water performance of ducted propellers with a panel method, *J. Mar. Sci. Eng.* 6 (2018) 27.
- [6] S.H. Rhee, S. Joshi, Computational validation for flow around a marine propeller using unstructured mesh based Navier-Stokes solver, *JSME Int. J. Ser. B: Fluids Therm. Eng.* 48 (2005) 562–570.
- [7] S. Brizzolara, D. Villa, S. Gaggero, A systematic comparison between RANS and panel methods for propeller analysis, Proc. of 8th International Conference on Hydrodynamics, Nantes, France, 2008.
- [8] M. Hoekstra, A RANS-based analysis tool for ducted propeller systems in open water condition, *Int. Shipbuild. Prog.* 53 (2006) 205–227.
- [9] D. Bertetta, S. Brizzolara, E. Canepa, S. Gaggero, M. Viviani, EFD and CFD characterization of a CLT propeller, *Int. J. Rotating Mach.* (2012).
- [10] S.A. Kinnas, C.-H. Jeon, J. Purohit, Y. Tian, Prediction of the unsteady cavitating performance of ducted propellers subject to an inclined inflow, International Symposium on Marine Propulsors SMP, volume 13 (2013).
- [11] S. Majdfar, H. Ghassemi, H. Forouzan, A. Ashrafi, Hydrodynamic prediction of the ducted propeller by CFD solver, *J. Mar. Sci. Technol.* 25 (2017) 268–275.
- [12] G. Kuiper, Scale effects on propeller cavitation inception, 12th Symposium on Naval Hydrodynamics (1978) 401–429.
- [13] H. Yao, H. Zhang, Numerical simulation of boundary-layer transition flow of a model propeller and the full-scale propeller for studying scale effects, *J. Mar. Sci. Technol.* (2018) 1–15.
- [14] A. Bhattacharyya, V. Krasilnikov, S. Steen, Scale effects on open water characteristics of a controllable pitch propeller working within different duct designs, *Ocean Eng.* 112 (2016) 226–242.
- [15] S.-B. Müller, M. Abdel-Maksoud, G. Hilbert, Scale effects on propellers for large container vessels, First International Symposium on Marine Propulsors (2009).
- [16] R.B. Langtry, F.R. Menter, S.R. Likki, Y.B. Suzen, P.G. Huang, S. Völker, A correlation-based transition model using local variables—Part II: Test cases and industrial applications, *J. Turbomach.* 128 (2006) 423–434.
- [17] P. Malan, K. Suluksa, E. Juntaras, Calibrating the $\gamma - Re_{\theta}$ transition model for commercial CFD, Proceedings of the 47th AIAA Aerospace Sciences Meeting Including the New Horizons Forum and Aerospace Exposition (2009) 1–20.
- [18] Siemens, 2017. StarCCM+ 12.04.011 Documentation. <https://thesteveportals.siemens.com/>.
- [19] A. Bhattacharyya, J.C. Neitzel, S. Steen, M. Abdel-Maksoud, V. Krasilnikov, Influence of flow transition on open and ducted propeller characteristics, Fourth International Symposium on Marine Propulsors, Austin, Texas, USA, 2015.
- [20] J.M. Baltazar, D. Rijkem, J.F. de Campos, On the use of the $\gamma - Re_{\theta}$ transition model for the prediction of the propeller performance at model-scale, *Ocean Eng.* 170 (2018) 6–19.
- [21] X. Wang, K. Walters, Computational analysis of marine-propeller performance using transition-sensitive turbulence modeling, *J. Fluids Eng.* 134 (2012) 071107.
- [22] L. Xu, E. Baglietto, S. Brizzolara, Extending the applicability of RANS turbulence closures to the simulation of transitional flow around hydrofoils at low Reynolds number, *Ocean Eng.* 164 (2018) 1–12.
- [23] F.R. Menter, R.B. Langtry, S.R. Likki, Y.B. Suzen, P.G. Huang, S. Völker, A correlation-based transition model using local variables—Part I: Model formulation, *J. Turbomach.* 128 (2006) 413–422.
- [24] F.R. Menter, Two-equation eddy-viscosity turbulence models for engineering applications, *AIAA J.* 32 (1994) 1598–1605.
- [25] K. Suluksa, P. Dechaumphai, E. Juntaras, Correlations for modeling transitional boundary layers under influences of freestream turbulence and pressure gradient, *Int. J. Heat Fluid Flow* 30 (2009) 66–75.
- [26] R.B. Langtry, A correlation-based transition model using local variables for unstructured parallelized CFD codes. Ph.D. Thesis, University of Stuttgart, 2006.
- [27] M.W.C. Oosterveld, Ducted propeller characteristics, RINA Symposium on Ducted Propellers (1973).
- [28] G. Kuiper, Cavitation inception on ship propeller models. Ph.D. Thesis, TU Delft, Delft University of Technology, 1981.
- [29] J. Baltazar, D. Rijkem, J.A.C. Falcao de Campos, J. Bosschers, A comparison of panel method and RANS calculations for a ducted propeller system in open-water, Third International Symposium on Marine Propulsors (SMP2013), Launceston, Tasmania, Australia, 2013.